
Filament recycling is necessary for sustained contractile flows in a model actomyosin cortex

William M McFadden¹, Patrick M McCall², Edwin M Munro^{3,*}

1 Biophysical Sciences Program, University of Chicago, Chicago, IL, USA

2 Department of Physics, University of Chicago, Chicago, IL, USA

3 Department of Molecular Genetics and Cell Biology, University of Chicago, Chicago, IL, USA

* emunro@uchicago.edu

Abstract

Actomyosin-based cortical flow is a fundamental engine for cellular morphogenesis. Cortical flows are generated by cross-linked networks of actin filaments and myosin motors, in which active stress produced by motor activity is opposed by passive resistance to network deformation. Continuous flow requires local remodeling through crosslink unbinding and and/or filament disassembly. But how local remodeling tunes stress production and dissipation, and how this in turn shapes long range flow, remains poorly understood. Here we study a computational model that captures minimal requirements for production and dissipation of contractile stress during cortical flow, namely asymmetric filament compliance, spatial heterogeneity of motor activity, reversible cross-links and filament turnover. We use this model to explore how the sustained production of active stress and passive resistance to deformation depend, individually, on cross-link dynamics and filament turnover. Then we explore how these dependencies combine to determine overall rates of cortical flow. Our analysis predicts that filament turnover is required to maintain active stress against external resistance and steady state flow in response to external stress. Steady state stress increases with filament lifetime up to a characteristic time τ_{max} , then decreases with lifetime above τ_{max} . Effective viscosity increases with filament lifetime up to a characteristic time τ_c , and then becomes independent of filament lifetime and sharply dependent on crosslink dynamics. These individual dependencies of active stress and effective viscosity define multiple regimes of steady state flow. In particular our model predicts the existence of a regime, when filament lifetimes are shorter than both τ_c and τ_{max} , in which dependencies of effective viscosity and steady state stress cancel one another, such that flow speed is insensitive to filament turnover, and shows simple dependence on motor activity and crosslink dynamics. These results provide a framework for understanding how animal cells tune cortical flow through local control of network remodeling.

Author Summary

In this paper, we develop and analyze a minimal model for a 2D network of cross-linked actin filaments and myosin motors, representing the cortical cytoskeleton of eukaryotic cells. We implement coarse-grained representations of force production by myosin motors and stress dissipation through an effective cross-link friction and filament

1
2
3
4

turnover. We use this model to characterize how the sustained production of active stress, and the steady dissipation of elastic stress, depend individually on motor activity, effective cross-link friction and filament turnover. Then we combine these results to gain insights into how these microscopic parameters control steady state flow produced by asymmetric distributions of motor activity. Our results provide a framework for understanding how local modulation of microscopic interactions within contractile networks control macroscopic quantities like active stress and effective viscosity to control cortical deformation and flow at cellular scales. insight on potential microscopic control parameters governing broad qualitative differences in 2D active networks.

Introduction

Cortical flow is a fundamental and ubiquitous form of cellular deformation that underlies cell polarization, cell division, cell crawling and multicellular tissue morphogenesis [Bray and White, 1988, Hird and White, 1993, Benink et al., 2000, Wilson et al., 2010, Munjal et al., 2015]. These flows originate within a thin layer of cross-linked actin filaments and myosin motors, called the actomyosin cortex, that lies just beneath the plasma membrane [Salbreux et al., 2012]. Local forces produced by bipolar myosin filaments are integrated within cross-linked networks to build macroscopic contractile stress [Murrell et al., 2015, Bendix et al., 2008, Janson et al., 1991]. At the same time, cross-linked networks resist deformation and this resistance must be dissipated by network remodeling to allow macroscopic deformation and flow. How force production and dissipation depend on motor activity, network architecture and remodeling remains poorly understood.

One successful approach to modeling cortical flow has relied on coarse-grained phenomenological descriptions of actomyosin networks as active fluids, whose motions are driven by gradients of active contractile stress and opposed by an effectively viscous resistance [Mayer et al., 2010]. In these models, spatial variation in active stress is typically assumed to reflect spatial variation in motor activity and force transmission, while viscous resistance is assumed to reflect the internal dissipation of elastic resistance due to local remodeling of filaments and/or cross-links [Bois et al., 2011]. By coupling an active fluid description to simple kinetic models for network assembly and disassembly and assuming local dependencies of active stress and effective viscosity on e.g myosin density and turnover rates, it has been possible to reproduce spatiotemporal dynamics of cortical flow observed during polarization [Mayer et al., 2010], cell division [Turlier et al., 2014, Salbreux et al., 2009], cell motility [Keren et al., 2009, Marchetti et al., 2013] and tissue morphogenesis [Heisenberg and Bellaïche, 2013]. However, it remains a key challenge to connect this coarse-grained description of cortical flow to the microscopic origins of force generation and dissipation within cross-linked actomyosin networks.

Studies in living cells reveal fluid-like stress relaxation on timescales of 10-100s of seconds [Mayer et al., 2010, Hird and White, 1993, Bray and White, 1988, Hochmuth, 2000, Evans and Yeung, 1989, Bausch et al., 1998], which is thought to arise through a combination of cross link unbinding and actin filament turnover [De La Cruz and Gardel, 2015, De La Cruz, 2009, Salbreux et al., 2012]. Theoretical [Broedersz et al., 2010, Müller et al., 2014] and computational [Kim et al., 2011, Lieleg et al., 2009, Lieleg and Bausch, 2007] studies reveal that cross-link unbinding can endow actin networks with complex time-dependent viscoelasticity. However, while *in vitro* studies confirm that cross-link unbinding is sufficient for viscous relaxation (creep) on very long timescales, this is unlikely to account for the rapid cortical deformation and flow observed in living cells [Wachsstock et al., 1994, Lieleg et al., 2008, Lieleg et al., 2009, Yao et al., 2011, Liu et al., 2007]. In contrast, far less is known about the

contributions of actin turnover to network relaxation. Experimental studies in living cells reveal rapid turnover of cortical actin filaments on timescales of 10-100 seconds [?, Fritzsche et al., 2013, Fritzsche et al., 2016, Carlsson, 2010, Lai et al., 2008]. Perturbing turnover can lead to changes in cortical mechanics and in the rates and patterns of cortical flow [Van Goor et al., 2012, Fritzsche et al., 2016]. However, the specific contributions of actin turnover to stress relaxation and how this depends on network architecture have received little experimental or theoretical attention.

Recent work has also begun to reveal mechanisms for active stress generation in disordered actomyosin networks. Theoretical studies suggest that spatial heterogeneity in motor activity along individual filaments, and asymmetrical filament compliance (stiffer in extension than in compression), are sufficient for macroscopic contraction [Lenz et al., 2012, Lenz, 2014], although other routes to contractility may also exist [Lenz, 2014]. *in vitro* studies confirm that local interactions among actin filaments and myosin motors are sufficient to drive macroscopic contraction of disordered networks [Murrell and Gardel, 2012], and support a mechanism based on asymmetrical filament compliance and filament buckling. In these studies, the filaments were preassembled, and network contraction was transient, because of irreversible network collapse [Alvarado et al., 2013], or buildup of elastic resistance [Murrell and Gardel, 2014], or because network rearrangements (polarity sorting) dissipate the potential to generate contractile force [Ennomani et al., 2016, Reymann et al., 2012, Nedelec et al., 1997, Surrey et al., 2001]. This suggests that network turnover may play an essential role(s) in allowing sustained production of contractile force. Recent theoretical and modeling studies have begun to explore how this might work [Hiraiwa and Salbreux, 2015, Mak et al., 2016, Zumdieck et al., 2007], and to explore dynamic behaviors that can emerge in contractile material with turnover [Salbreux et al., 2009, Dierkes et al., 2014]. Nevertheless, it remains a significant challenge to understand how force production and dissipation depend individually on the local interplay of network architecture, motor activity and filament turnover, and how these dependencies combine to mediate tunable control of long range cortical flow.

Here, we address this challenge by constructing and analysing a minimal computational model that bridges between the microscopic description of cross-linked actomyosin networks and the coarse grained description of an active fluid. We represent actin filaments as simple springs with asymmetric compliance; we represent dynamic binding/unbinding of elastic cross-links as molecular friction [Vanossi et al., 2013, Spruijt et al., 2010, Filippov et al., 2004] at all filament crossover points; we represent motor activity as force coupling on a subset of filament cross-over points with a simple linear force/velocity relationship [Banerjee et al., 2011]. Finally, we model filament turnover by allowing entire filaments to appear with a fixed probability per unit area and disappear with fixed probabilities per unit time. We use this model first to characterize the passive response of a cross-linked network to externally applied stress, then the buildup and maintenance of active stress against an external resistance, and finally the steady state flows produced by an asymmetric distribution of active motors in which active stress and passive resistance are dynamically balanced across the network. Our results reveal how network remodeling tune cortical flow through simultaneous effects on active force generation and passive resistance to network deformation.

Models

Our goal in this study was to build and analyse a “minimal model” that is detailed enough to capture essential microscopic features of cross-linked actomyosin networks

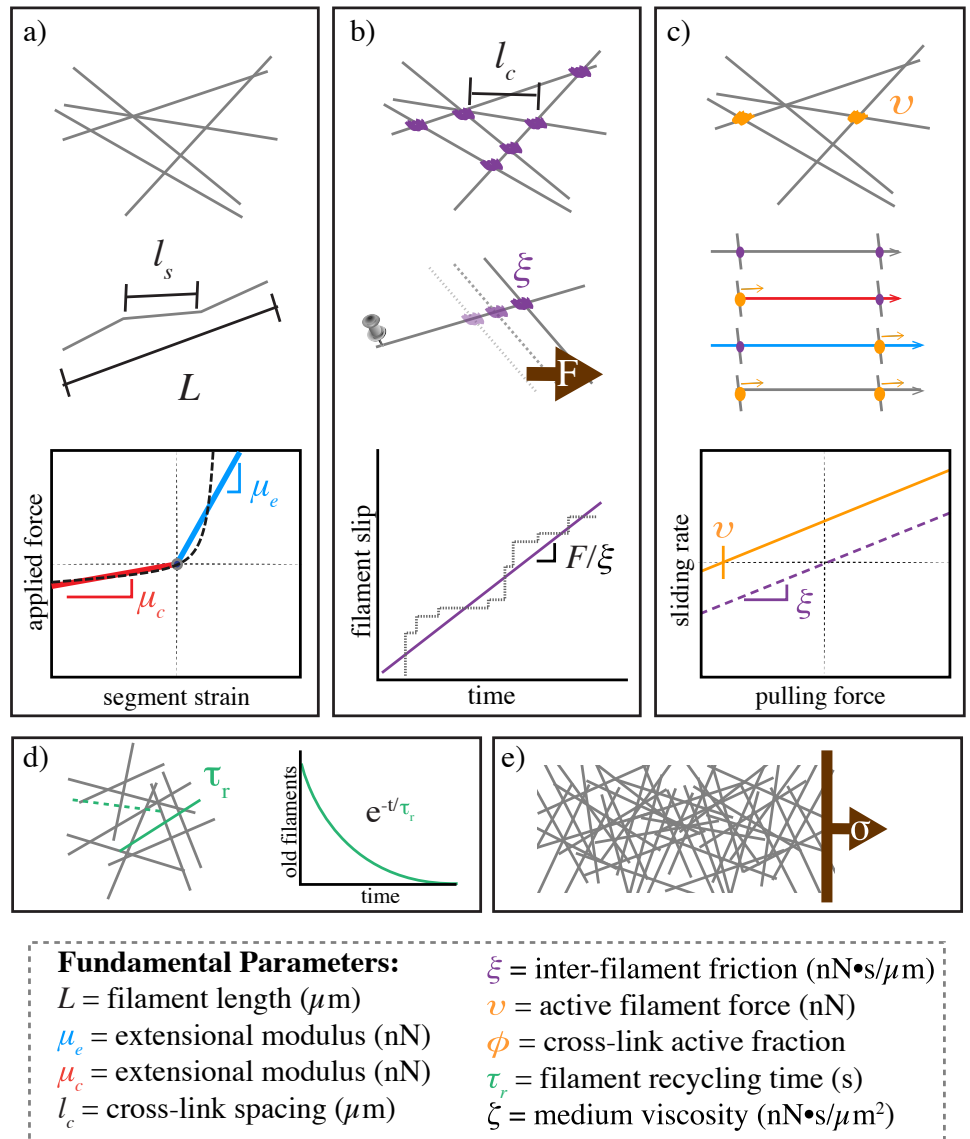


Figure 1. Schematic of modeling framework. a) Filament segments are represented as simple linear springs that are stiffer in extension than in compression. b) Cross-linking is assumed to occur at all filament crossings and is represented by an effective drag, such that their relative motion is proportional to any applied force. c) Motor activity manifests as a linear force-velocity relationship with a fixed force at zero velocity. Spatial heterogeneity of motor activity is implemented by imposing motor activity at a fixed fraction of filament crossover points, resulting in variation in the magnitudes of compressive vs extensile vs translational forces along individual filament segments. d) Filament turnover. Whole filaments disappear at a constant rate and new filaments appear with random location and orientation at the constant rate per unit area, such that entire network refreshes on a characteristic timescale τ .

(actin filaments with asymmetric compliance, dynamic cross-links, active motors and continuous filament turnover), but simple enough to allow systematic exploration of how these microscopic features control macroscopic deformation and flow. We focus on

2D networks because they capture a reasonable approximation of the quasi-2D cortical actomyosin networks that govern flow and deformation in many eukaryotic cells [Mayer et al., 2010, Chugh et al., 2016], or the quasi-2D networks studied recently *in vitro* [Murrell and Gardel, 2012, Sanchez et al., 2012].

We model each filament as an oriented elastic spring with relaxed length l_s . A filament is defined by its endpoints, or nodes, with positions \mathbf{x}_i and \mathbf{x}_{i+1} marking the (-) and (+) ends respectively. The index i enumerates over all nodes of all filaments, and we refer to the filament connecting nodes i and $i + 1$ as filament i . We define $\hat{\mathbf{u}}_i$ to be the unit vector oriented along filament i

Asymmetric filament compliance

Local deformation of filament i gives rise to an elastic force:

$$\mathbf{F}_{i,i+1}^\mu = \mu \gamma_i \hat{\mathbf{u}}_i \quad (1)$$

where $\gamma_i = (|\mathbf{x}_{i-1} - \mathbf{x}_i| - l_s)/l_s$ is the strain on segment i , and the elastic modulus μ is a composite quantity that represents both filament and cross-linker compliance as in the effective medium theory of Broedersz and colleagues [Broedersz et al., 2009]. and To model asymmetric filament compliance, we set $\mu = \mu_e$ if the strain is positive (extension), and $\mu = \mu_c$ if the strain is negative (compression). In the limit of highly rigid cross-links and flexible filaments, our model approaches the pure semi-flexible filament models of [Head et al., 2003, Wilhelm and Frey, 2003]. In the opposite limit (nearly rigid filaments and highly flexible cross links), our model approaches that of [Broedersz et al., 2009] in small strain regimes before any nonlinear cross link stiffening.

The total elastic force on a filament node i can be written as:

$$\mathbf{F}_i^{\text{elas}} = \mathbf{F}_{i,i+1}^\mu - \mathbf{F}_{i-1,i}^\mu \quad (2)$$

Drag-like coupling between overlapping filaments

Previous models represent cross-linkers as elastic connections between pairs of points on neighboring filaments that appear and disappear with either fixed or force-dependent probabilities [Kim et al., 2011, Broedersz et al., 2009]. Here, we introduce a coarse-grained representation of crosslink dynamics by introducing an effective drag force that couples every pair of overlapping filaments, and which represents a molecular friction arising from the time-averaged contributions of many individual transient crosslinks. This coarse-grained approximation has been shown to be adequate in the case of ionic cross-linking of actin [Ward et al., 2015, Chandran and Mofrad, 2010], and has been used to justify simple force-velocity curves for myosin bound filaments in other contexts [Banerjee et al., 2011].

To implement coupling through effective drag, for any pair of overlapping filaments j and k , we write the drag force on filament j as:

$$\mathbf{F}_{j,k}^\xi = -\xi(\mathbf{v}_j - \mathbf{v}_k) \quad (3)$$

where ξ is the drag coefficient and \mathbf{v}_j , \mathbf{v}_k are the average velocities of filaments j and k . We apportion this drag force to the two endpoints (nodes j , $j+1$) of filament j as follows: If $\mathbf{x}_{j,k}$ is the position of the filament overlap, then we assign $(1 - \lambda_{j,k})\mathbf{F}_{j,k}^\xi$ to node j and $\lambda_{j,k}\mathbf{F}_{j,k}^\xi$ to node $j+1$, where $\lambda_{j,k} = \frac{|\mathbf{x}_{j,k} - \mathbf{x}_j|}{|\mathbf{x}_{j+1} - \mathbf{x}_j|}$.

The total crosslink coupling force on node i due overlaps along filament i and $i-1$ can then be written:

$$\mathbf{F}_i^{\text{xl}} = \sum_j (1 - \lambda_{i,j}) \mathbf{F}_{i,j}^{\xi} + \sum_k \lambda_{i-1,k} \mathbf{F}_{i-1,k}^{\xi} \quad (4)$$

where the sums are taken over all filaments j and k that overlap with filaments i and $i-1$ respectively.

This model assumes a linear relation between the drag force and the velocity difference between attached filaments. Although non-linearities can arise through force dependent detachment kinetics and/or non-linear force extension of cross-links, we assume here that these non-linear effects are of second or higher order.

Active coupling for motor driven filament interactions

To add motor activity at the point of overlap between two filaments j and k ; for each filament in the pair, we impose an additional force of magnitude v , directed towards its (-) end:

$$\mathbf{F}_i^v = v \hat{\mathbf{u}}_i \quad (5)$$

and we impose an equal and opposite force on its overlapping partner. We distribute these forces to filament endpoints as described above for crosslink coupling forces. Thus, the total force on node i due to motor activity can be written as:

$$\mathbf{F}_i^{\text{motor}} = v \sum_j (1 - \lambda_{i,j}) (\hat{\mathbf{u}}_i - \hat{\mathbf{u}}_j) q_{i,j} + v \sum_k (\lambda_{i-1,k}) (\hat{\mathbf{u}}_{i-1} - \hat{\mathbf{u}}_k) q_{i-1,k} \quad (6)$$

where j and k enumerate over all filaments that overlap with filaments i and $i-1$ respectively, and $q_{j,k}$ equals 0 or 1 depending on whether there is an “active” motor at this location. To model dispersion of motor activity, we set $q_{i,j} = 1$ on a randomly selected subset of cross-link points at the beginning of the simulation, such that $\bar{q} = \phi$, where \bar{q} indicates the mean of q .

To write the full equation of motion for a network of actively and passively coupled elastic filaments, we assume the low Reynold’s number limit in which inertial forces are negligible and we equate the sum of all forces acting on each filament node to zero to obtain:

$$0 = -l_s \zeta \mathbf{v}_i - \mathbf{F}_i^{\text{xl}} + \mathbf{F}_i^{\text{elas}} + \mathbf{F}_i^{\text{motor}} \quad (7)$$

where the first term represents the hydrodynamic drag on the pair of half-filament adjoining node i , with respect to motion against the surrounding fluid and ζ is the drag coefficient.

2D network formation

We used a mikado model approach [Unterberger and Holzapfel, 2014] to initialize a minimal network of overlapping unstressed linear filaments in a rectangular 2D domain. We generate individual filaments by laying down straight lines of length, L , with random position and orientation. We define the density using the average distance between cross-links along a filament, l_c . A simple geometrical argument can then be used to derive the number of filaments filling a domain as a function of L and l_c [Head et al., 2003]. Here, we use the approximation that the number of filaments needed to tile a rectangular domain of size $D_x \times D_y$ is $2D_x D_y / L l_c$, and that the length density is therefore simply, $2/l_c$.

Modeling filament turnover

In living cells, actin filament assembly is governed by multiple factors that control filament nucleation, branching and elongation. Likewise filament disassembly is governed by multiple factors that promote filament severing and monomer dissociation at filament ends. Here, we focus on a lowest order model for filament recycling in which entire filaments appear with a fixed rate per unit area, k_{app} and disappear at a rate $k_{diss}\rho$, where ρ is a filament density. With this assumption, in the absence of network deformation, the density of filaments will equilibrate to a steady state density, k_{app}/k_{diss} , with time constant $\tau_r = 1/k_{diss}$. In deforming networks, the density will be set by a competition between strain thinning ($\gamma > 0$) or thickening ($\gamma < 0$), and density equilibration via turnover. To implement this model, at fixed time interval $\tau_s < 0.01 \cdot \tau_r$ (i.e. 1% of the equilibration time), we selected a fraction, τ_s/τ_r , of existing filaments (i.e. less than 1% of the total filaments) for degradation. We then generated a fixed number of new unstrained filaments $k_{app}\tau_s D_x D_y$ at random positions and orientations within the original domain. This method ensures that there is a constant number of filaments within the domain of analysis $0 \leq y \leq D_y; 0 \leq x \leq D_x$ throughout the simulation. We refer to this continuous turnover as filament recycling, to $k_{diss} = 1/\tau_r$ as the recycling rate, and to τ_r as the recycling time.

Simulation methods

Further details regarding our simulation approach and references to our code can be found in the Appendix. Briefly, equations 1-7 define a coupled system of ordinary differential equations that can be written in the form:

$$\mathbf{A} \cdot \dot{\mathbf{x}} = \mathbf{f}(\mathbf{x}) \quad (8)$$

where \mathbf{x} is a vector of segment endpoint (node) positions, $\dot{\mathbf{x}}$ their velocities, \mathbf{A} is a matrix with constant coefficients that represent crosslink coupling forces between overlapping filament segments, and $\mathbf{f}(\mathbf{x})$ represents the active (motor) and elastic forces filament nodes. We smoothed all filament interactions, force fields, and constraints over small regions such that the equations contained no sharp discontinuities. We numerically integrate this system of equations to find the time evolution of the positions of all filament endpoints. We generate a network of filaments with random positions and orientations as described above within a domain of size D_x by D_y . For all simulations, we imposed periodic boundaries in the y-dimension. To impose an extensional stress, we constrained all filament segment endpoints within a fixed distance $0.05 \cdot D_x$ from the left edge of the domain to be non-moving, then we imposed a rightwards force on all segment endpoints within a distance $0.05 \cdot D_x$ from the right edge of the domain. To simulate free contraction, we removed all constraints at domain boundaries; to assess buildup and maintenance of contractile stress under isometric conditions, we used periodic boundary conditions in both x and y dimensions.

We measured the local velocity of the network at different positions along the axis of deformation as the mean velocity of all filament segments intersecting that position; we measured the internal network stress at each position by summing the axial component of the tensions on all filament segments intersecting that position, and dividing by network height; finally, we measured network strain rate as the average of all filaments velocities divided by their positions.

We explored parameter space around an estimate of biologically relevant parameter values given in Table 1.

Table 1. Simulation Parameter Values

parameter	symbol	physiological estimate
extensional modulus	μ_e	$1nN$
compressional modulus	μ_c	$0.01nN$
cross-link drag coefficient	ξ	<i>unknown</i>
solvent drag coefficient	ζ	$0.0005 \frac{nNs}{\mu m^2}$
filament length	L	$5\mu m$
cross-link spacing	l_c	$0.5\mu m$
active filament force	v	$0.1nN$
active cross-link fraction	ϕ	$0.1 < 0.9$
domain size	$D_x \times D_y$	$20 \times 50\mu m$

Results and Discussion

To goal of this study is to understand how cortical flow is shaped by the simultaneous dependencies of active stress and effective viscosity on filament turnover, crosslink drag and on “network parameters” that control filament density, elasticity and motor activity. We approach this in three steps: First, we analyze the passive deformation of a cross-linked network in response to an externally applied stress; we identify regimes in which the network response is effectively viscous and characterize the dependence of effective viscosity on network parameters and filament turnover. Second, we analyze the buildup and dissipation of active stress in cross-linked networks with active motors, as they contract against an external resistance; we identify conditions under which the network can produce sustained stress at steady state, and characterize how steady state stress depends on network parameters and filament turnover. Third, we confirm that the dependencies of active stress and effective viscosity on network parameters and filament turnover are sufficient to predict the dynamics of networks undergoing steady state flow in response to spatial gradients of motor activity.

Filament turnover allows and tunes effectively viscous steady state flow.

Networks with passive cross-links and no filament turnover undergo three stages of deformation in response to an extensional force. To characterize the passive response of a cross-linked filament network without filament recycling, we simulated a simple uniaxial strain experiment in which we pinned the network at one end, imposed an external stress at the opposite end, and then quantified network strain and internal stress as a function of time. The typical response occurred in three qualitatively distinct phases (Figure 2a,c). At short times the response was viscoelastic, with a rapid buildup of internal stress and a rapid \sim exponential approach to a fixed strain (Figure S1 Figa), which represents the elastic limit in the absence of cross-link slip predicted by [Head et al., 2003]. At intermediate times, the response was effectively viscous; internal stress remained constant while the network continued to deform slowly and continuously with nearly constant strain rate (shown as dashed line in Fig 2c) as filaments slip past one another against the effective cross-link drag. In this regime, we can quantify effective viscosity, η_c , as the ratio of applied stress to the measured strain rate. Finally, as the network strain approached a critical value ($\sim 30\%$ for the simulation in Figure 2), strain thinning lead to decreased network connectivity, local tearing, and rapid acceleration of the network deformation (see inset in Figure 2c).

Network architecture sets the rate and timescales of deformation. To characterize how effective viscosity and the timescale for transition to effectively viscous

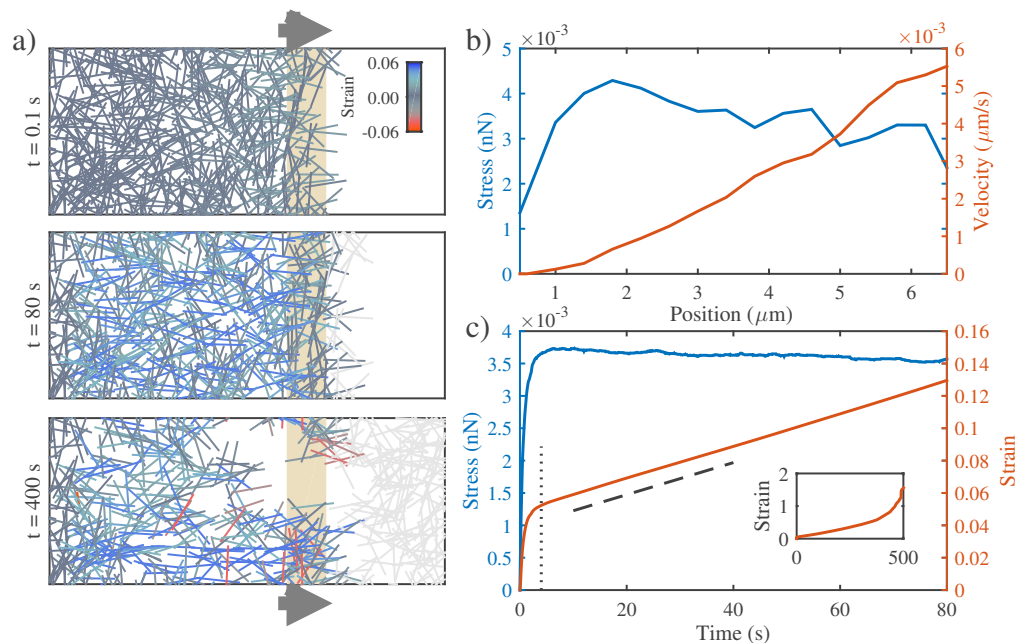


Figure 2. Networks with passive cross-links and no filament turnover undergo three stages of deformation in response to an extensional stress. **a)** Three successive time points from a simulation of a $4 \times 6.6 \mu\text{m}$ network deforming under an applied stress of $0.005 \text{ nN}/\mu\text{m}$ (stress is applied to filaments in the region indicated by the tan bar). In this and all subsequent figures, filaments are color-coded with respect to state of strain (blue = tension, red = compression). Network parameters: $L = 1 \mu\text{m}$, $l_c = 0.3 \mu\text{m}$, $\xi = 100 \text{ nN} \cdot \text{s}/\mu\text{m}$. **b)** Mean filament stress and velocity profiles for the network in (a) at $t = 88 \text{ s}$. Note that the stress is nearly constant and the velocity is nearly linear as predicted for a viscous fluid under extension. **c)** Plots of the mean stress and strain vs time for the simulation in (a), illustrating the three stages of deformation: (i) A fast initial phase accompanies rapid buildup of internal network stress; (ii) after a characteristic time τ_c (indicated by vertical dotted line) the network deforms like a material with a constant effective viscosity, η_c , as indicated by the slope of the dashed line; (iii) at long times, the network undergoes strain thinning and tearing (see inset)

behavior depend on network architecture and cross-link dynamics, we simulated a uniaxial stress test, holding the applied stress constant, while varying filament length L , density l_c , elastic modulus μ_e and cross link drag ξ (see S1 Table). We measured the elastic modulus, G_0 , the effective viscosity, η_c , and the timescale τ_c for transition from viscoelastic to effectively viscous behavior, and compared these to theoretical predictions. We observed a transition from viscoelastic to effectively viscous deformation for the entire range of parameter values that we sampled. Our estimate of G_0 from simulation agreed well with the closed form solution $G_0 \sim \mu/l_c$ predicted by a previous theoretical model [Head et al., 2003] for networks of semi-flexible filaments with irreversible cross-links (Figure 3b).

A simple theoretical analysis of filament networks with frictional cross link slip, operating in the intermediate viscous regime (shown in S1 Text), predicted that the effective viscosity η_c should be proportional to the cross-link drag coefficient and to the square of the number of cross-links per filament:

$$\eta_c = \frac{\pi}{4} \xi \left(\frac{L}{l_c} - 1 \right)^2 \quad (9)$$

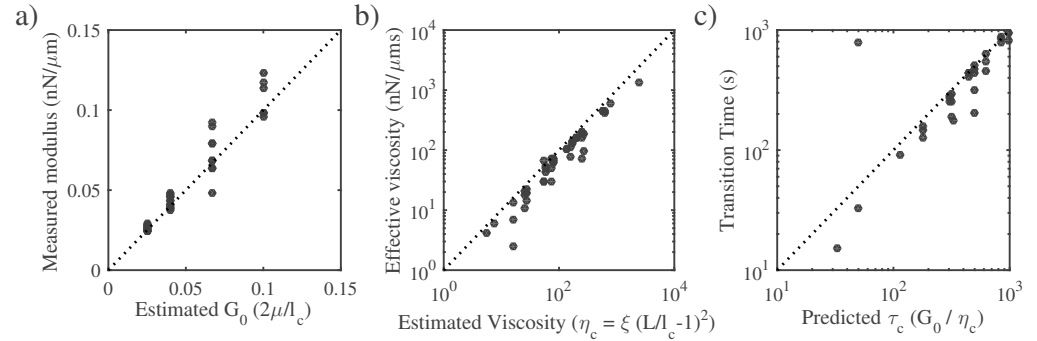


Figure 3. Network architecture sets the rate and timescales of deformation. **a)** Elastic modulus of filament networks matches with prediction. **b)** The effective viscosity depends on the drag coefficient and the density of the network. Data points are the normalized effective viscosity from simulations (effective viscosity measured in fluid phase divided by the cross link friction coefficient) vs the number of cross links per filament ($L/l_c - 1$). Dotted line indicates the relationship predicted by a simple theory, $\eta_c = \xi(L/l_c - 1)^2$. **c)** The transition to viscous behavior occurs at a characteristic time, τ_c , given by the ratio of modulus G_0 to effective viscosity, η_c .

As shown in Figure 3b, our simulations agree well with this prediction for a large range of sampled network parameters. Finally, for many linear viscoelastic materials, the ratio of effective viscosity to the elastic modulus sets the timescale for transition from elastic to viscous behavior [McCrum et al., 1997]. Combining our approximations for G_0 and η_c , we predict a transition time, $\tau_c \approx L^2 \xi / l_c \mu$. Measuring the time at which the strain rate became nearly constant (i.e. $\gamma \sim t^n$ with $n > 0.8$) yields an estimate of τ_c that agrees well with this prediction over the entire range of sampled parameters (Figure 3c). Thus the passive response of filament networks with frictional cross link drag is well-described on short (viscoelastic) to intermediate (viscous) timescales by three quantities with well-defined dependencies on network parameters: an elastic modulus G_0 , an effective viscosity η_c , and a transition timescale τ_c . However for these networks, strain thinning and network tearing limits the extent of viscous deformation to small strains.

Filament recycling allows continuous large-scale viscous flow and modulates effective viscosity. To explore how filament turnover shapes the passive network response to an applied force, we introduced a simple form of turnover in which entire filaments disappear at a rate $k_{diss}\rho$, where ρ is the filament density, and new unstrained filaments appear with a fixed rate per unit area, k_{app} . With these assumptions, in a non-deforming network, filament density should equilibrate to a steady state value, $\rho_0 = \frac{k_{app}}{k_{diss}}$, with time constant $\tau_r = 1/k_{diss}$; In a network deforming under extensional stress, the density should be set by a competition between strain thinning and density equilibration via turnover.

We simulated the uniaxial stress test for varying τ_r , while holding all other parameters fixed (Figure 4a-c). For large τ_r , as described above, the network thins and ultimately tears as it deforms. Decreasing τ_r decreased the rate of strain thinning and increased the time, and amount of strain, at which tearing occurs (EMM: need to show this in fig?). Below a critical value $\tau_r = \tau_{crit}$, strain thinning and tearing no

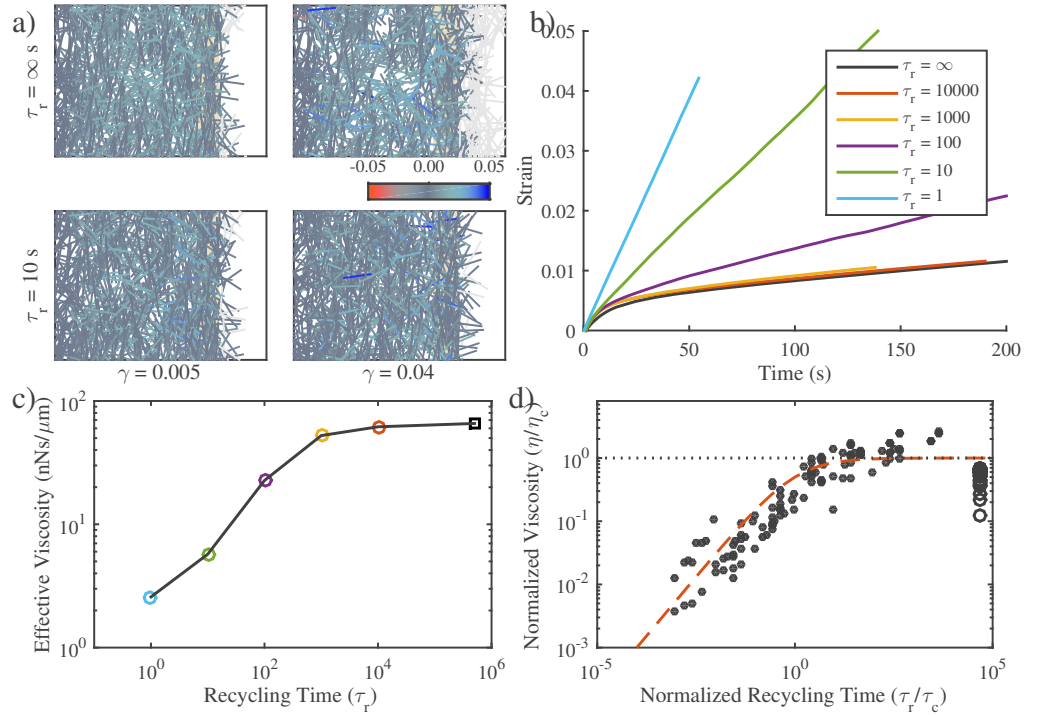


Figure 4. Filament recycling modulates effective viscosity in two regimes. **a)** Examples of $20 \times 12 \mu\text{m}$ network under $0.001 \text{ nN}/\mu\text{m}$ extensional stress with recycling ($\tau_r = 10 \text{ s}$) and without, ($\tau_r = \infty$). Both images are taken when the patches had reached a net strain of 0.04. For clarity, filaments that leave the domain of applied stress are greyed out. **b)** Strain curves for identical networks with varying levels of filament recycling. Network parameters: $L = 5 \mu\text{m}$, $l_c = 0.5 \mu\text{m}$, $\xi = 10 \text{ nN} \cdot \text{s}/\mu\text{m}$. **c)** Plotting the effective viscosity derived from the slopes of the lines in panel a. Square dot is the $\tau_r = \infty$ condition. **d)** Effective viscosities (normalized by the effective viscosity in the absence of recycling, η_c) as a function of the normalized recycling time. When the recycling timescale is significantly less than the passive relaxation timescale, the viscosity of the network becomes dependent on recycling time. Red dashed line indicates the approximation given in equation 12 for $m = 3/4$.

longer occur, and networks undergo steady state flow at constant density and strain rate. For $\tau_r < \tau_{crit}$, we observed two distinct steady state flow regimes: an intermediate turnover regime in which steady state strain rate remains constant with decreasing τ_r , and a high turnover regime in which the steady state strain rate decreases monotonically with further decreases in τ_r .

To understand what determines τ_{crit} , we consider a simple coarse grained model for how ρ changes as a function of filament assembly k_{ass} , filament disassembly $k_{diss}\rho$ and strain thinning $\dot{\gamma}\rho$. Using $\rho_0 = \frac{k_{ass}}{k_{diss}}$, $\tau_r = 1/k_{diss}$, and $\dot{\gamma} = \sigma/\eta_c$, we write:

$$\frac{d\rho}{dt} = \frac{1}{\tau_r} \left(\rho_0 - \rho - \frac{\sigma\tau_r}{\eta_c(\rho)} \rho \right) \quad (10)$$

where $\eta_c = \eta_c(\rho)$ on the right hand side reflects the dependence of effective viscosity on network density. The strength of this dependence determines whether a stable steady state, representing continuous flow, can exist. Using our theoretical formula for η_c , and invoking simple geometric arguments to relate cross link spacing (l_c) to filament density

(ρ), we can estimate the critical value of τ_r below which a stable steady state exists as a function of applied stress σ , cross link density $\frac{L}{l_c}$ and crosslink drag ξ :

$$\tau_{crit} = \frac{\xi \left(\sqrt{\frac{L}{l_c}} - 1 \right)^3}{\sigma}. \quad (11)$$

To understand how filament turnover and network properties shape steady state flow in the intermediate and high turnover regimes, we measured steady state response to uniaxial stress while varying filament length, stiffness and density; cross link friction and filament turnover times (Figure 4a,b). Strikingly, when we plotted the normalized effective viscosity ($\frac{\eta_r}{\eta_c}$ vs a normalized recycling rate ($\frac{\tau_r}{\tau_c}$) for all parameter values, the data collapsed onto a single curve, with a transition at $\tau_r \approx \tau_c$ between an intermediate turnover regime in which effective viscosity is independent of τ_r and an high turnover regime in which effective viscosity falls monotonically with decreasing $\left(\frac{\tau_r}{\tau_c}\right)$ (Figure 4c).

This biphasic dependence of effective viscosity on filament turnover can be understood intuitively as follows: As new filaments are born, they become progressively stressed as they stretch and reorient under local influence of surrounding filaments, eventually reaching an elastic limit where their contribution to resisting network deformation is determined by effective crosslink drag. The time to reach this limit is about the same as the time, τ_c , for an entire network of initially unstrained filaments to reach an elastic limit during the initial viscoelastic response to uniaxial stress, as shown in Figure 2b. For $\tau_r < \tau_c$, individual filaments do not have time, on average, to reach the elastic limit before turning over; thus the deformation rate is determined by the elastic resistance of partially strained filaments, which increases with lifetime up to $\tau_r = \tau_c$. For $\tau_r > \tau_c$, the deformation rate is largely determined by cross-link resistance to sliding of maximally strained filaments, and the effective viscosity is insensitive to further increase in τ_r .

In summary, our simulations predict that filament turnover allows networks to undergo viscous deformation indefinitely, without tearing, over a wide range of different effective viscosities and deformation rates. For $\tau_r < \tau_{crit}$, this behavior can be summarized by an equation of the form:

$$\eta = \frac{\eta_c}{1 + (\tau_c/\tau_r)^m} \quad (12)$$

For $\tau_r \gg \tau_c$, $\eta \approx \eta_c$: effective viscosity depends on crosslink density and effective crosslink drag, independent of changes in recycling rate. For $\tau_r \ll \tau_c$, effective viscosity is governed by the level of elastic stress on network filaments, and becomes strongly dependent on filament lifetime: $\eta \sim (\tau_r/\tau_c)^m$, with $m = 3/4$, although the origins of the $3/4$ scaling remain unclear.

These results complement and extend previous simulations of passive creep in cross-linked networks subjected to extensional stress [Kim et al., 2014]. Kim et al considered networks with irreversible cross links in which filaments undergo turnover by treadmilling; they identified two regimes of effectively viscous deformation: a “stress-dependent” regime in which filaments turnover before they become strained to an elastic limit and creep rate depends on applied stress and turnover rate; and a “stress-independent” regime in which filaments reach an elastic limit before turning over and creep rate depends only on the turnover rate, and is insensitive to variation in applied stress. The fast and slow turnover regimes we observe here correspond to the stress-dependent and independent regimes described by Kim et al, but with a key difference. Without filament turnover, Kim et al’s model predicts a network cannot that deform beyond its elastic limit. In contrast, our model predicts viscous flow at low turnover, governed by cross-link dominated effective viscosity. Thus our model provides

a self-consistent framework for understanding how crosslink unbinding and filament turnover contribute separately to viscous flow and connects these contributions directly to previous theoretical descriptions of cross-linked networks of semi-flexible filaments.

Filament recycling allows persistent stress buildup in active networks

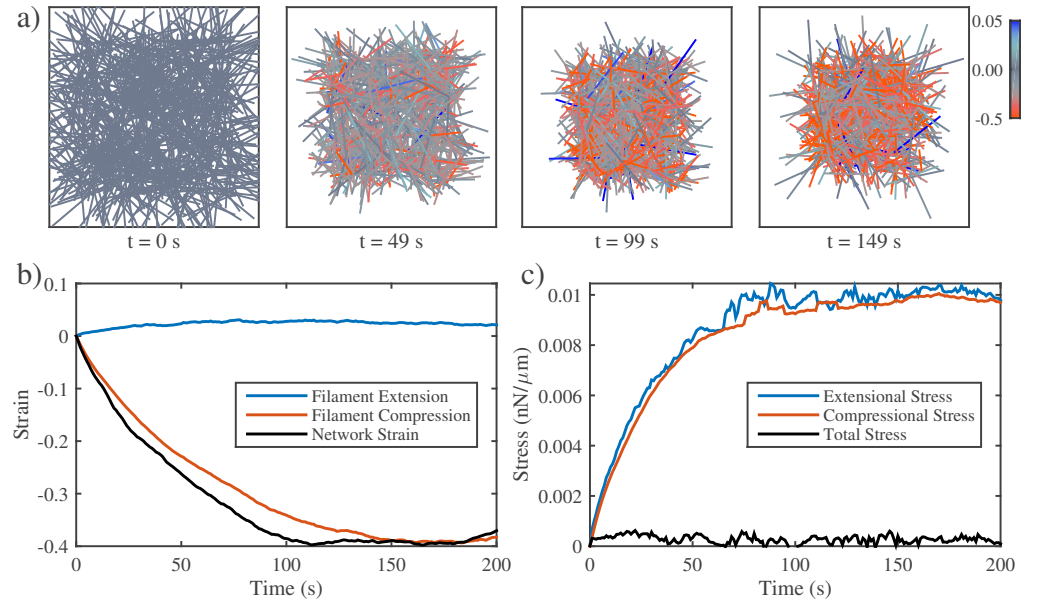


Figure 5. In the absence of filament recycling, active networks with free boundaries contract and then stall against passive resistance to network compression. **a)** Example of an active network contracting. Colors represent individual filament strain as in previous figures. Note the buildup of compressive stress as contraction approaches stall between 100 s and 150 s. Network parameters: $L = 5 \mu\text{m}$, $l_c = 0.3 \mu\text{m}$, $\xi = 1 \text{ nN} \cdot \text{s}/\mu\text{m}$, $v = 0.1 \text{ nN}$. **b)** Plots showing time evolution of total network strain and the average extensional (blue) or compressive (red) strain on individual filaments. **c)** Stress buildup in contracting network. Both extensional and compressive stress remain balanced in the contracting networks.

In the absence of filament recycling, active networks with free boundaries contract and then stall against passive resistance to network compression. Previous theoretical and experimental studies [Lenz et al., 2012, Murrell and Gardel, 2012, Koenderink et al., 2009] identified asymmetric filament compliance and spatial heterogeneity in motor activity as minimal requirements for macroscopic contraction of disordered networks. To confirm that our simple implementation of these two requirements (see Models section) is sufficient for macroscopic contraction, we simulated active networks that are unconstrained by external attachments, varying filament length, density, crosslink drag and motor activity. The result was qualitatively similar for all cases: Turning on motor activity in an initially unstrained network produced a rapid initial contraction, followed by a slower buildup of compressive stress (and strain) on individual filaments, and an \sim exponential approach to stall (Figure 5). The time to stall, τ_s , scaled as $L\xi/v$ (see S2 Figb), although the origins of this scaling relationship remain unclear. On even longer timescales, polarity sorting of individual filaments, as previously described [Reymann et al., 2012, Murrell and Gardel, 2014, Nedelec et al.,

1997, Surrey et al., 2001] lead to network expansion (see S2 Video).

During the rapid initial contraction, the increase in network strain closely matched the increase in mean compressive strain on individual filaments Figure 5b, as predicted theoretically [Lenz et al., 2012, Lenz, 2014] and observed experimentally [Murrell and Gardel, 2012]. Contraction required asymmetric filament compliance ($\frac{\mu_e}{\mu_c} > 1$) and spatial heterogeneity of motor activity ($\phi < 1$) as shown in S2 Fig. Thus our model captures a minimal mechanism for bulk contractility in disordered networks through asymmetric filament compliance and dispersion of motor activity. However, in the absence of turnover, contraction is limited by internal buildup of compressive resistance and the dissipative effects of polarity sorting.

Active networks can only exert a transient stress against a fixed boundary in the absence of filament recycling. During cortical flow, regions with high motor activity contract against a passive resistance from neighboring regions with lower motor activity. To understand how the active stresses driving cortical flow are shaped by motor activity and network remodeling, we analyzed the buildup and maintenance of contractile stress in active networks contracting against a rigid boundary. We simulated active networks contracting from an initially unstressed state against a fixed boundary (Figure 6a), and monitored the time evolution of mean extensional (blue), compressional (red) and total (black) stress on network filaments (Figure 6b). We focused initially on the scenario in which there is very slow filament turnover ($\tau_r = \infty$ or $\tau_r > 300\tau_{max}$), sampling a range of parameter values controlling filament length and density, motor activity, and crosslink drag.

We observed a similar behavior in all cases: total stress built rapidly to a peak value σ_{max} , and then decayed towards zero. The rapid initial increase in total stress was determined largely by the rapid buildup of extensional stress on a subset of network filaments (Figure 6 a,b $t = 10s$). The subsequent decay involved two different forms of local remodeling: under some conditions, e.g. for higher motor activity (e.g. Figure 6 a), the decay was associated with rapid local tearing and fragmentation, leading to global loss of network connectivity as described previously both in simulations ([Mak et al., 2016]) and *in vitro* experiments (EMM: cite Alverado 2013). However, for a large range of parameters, the decay in stress occurred with little or no loss of global connectivity (e.g. Figure 6 b), through a slow decrease in the average extensional stress, and a correspondingly slow increase in the compressional stress, on individual filaments (see Figure 6 d). These changes occur as local sliding and deformation of individual filaments leads to changes in connectivity that shift the balance of extensile vs compressive forces along individual filaments.

Sampling these dynamics over a large range of network parameters, and using dimensional analysis, we found that the peak stress occurred at a characteristic time, $\tau_{max} \sim L\xi/\sqrt{\mu_e v}$, as shown in Figure 6c. Although, the origins of this peculiar scaling are unclear, the measurement agrees with our intuitive predictions: The time to reach peak stress should increase with increased cross-link coupling (ξ) and filament length (L), and it should decrease with increasing filament stiffness (μ_e) and motor force (v).

Filament recycling allows networks to exert sustained stress on a fixed boundary. To understand how the dissipation of active stress might be relieved by filament turnover, we varied the rate of filament turnover, holding all other parameter values fixed, and monitored the buildup and dissipation of active stress in a network contracting against a fixed boundary from an initially unstressed state. We found that the peak stress σ_{max} decreased monotonically with increasing turnover (decreasing τ_r). However, steady state stress showed biphasic dependence on filament turnover, increasing initially with decreasing τ_r , and then falling off as $\tau_r \rightarrow 0$. Significantly, the

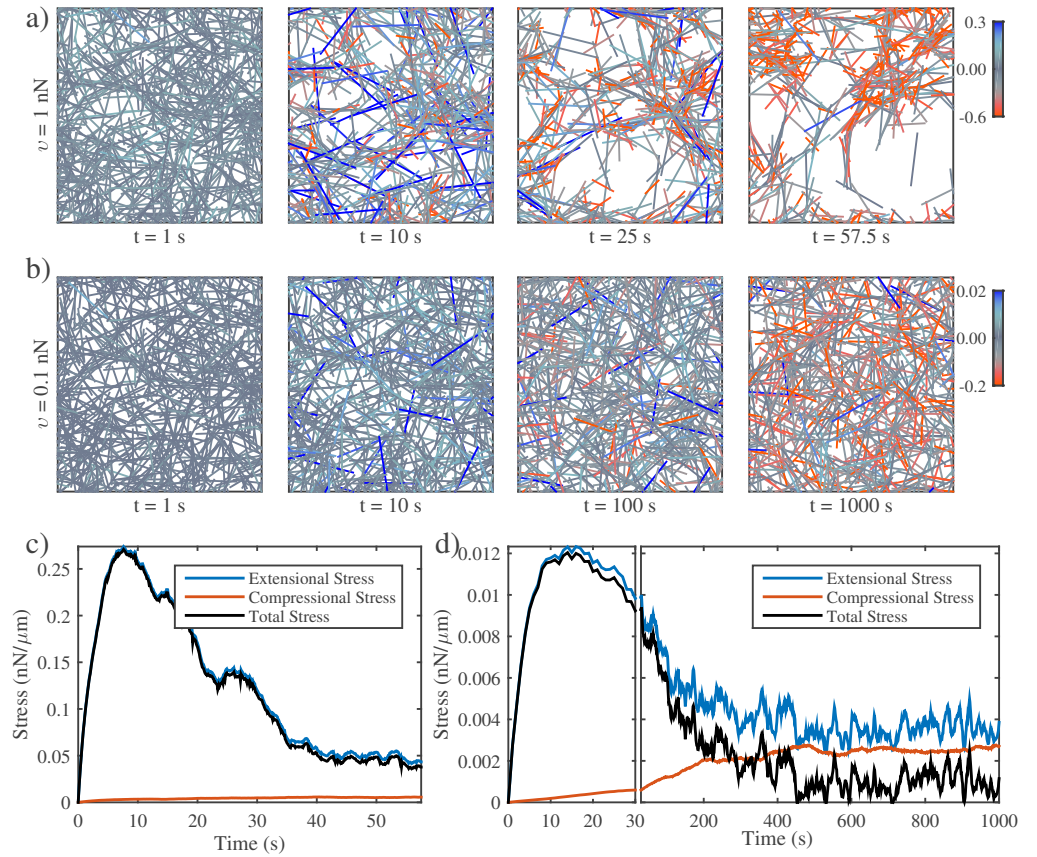


Figure 6. In the absence of filament recycling, active networks can only exert a transient force against a fixed boundary. **a)** Simulation of an active network with fixed boundaries illustrating progressive buildup of internal stress through local filament rearrangement and deformation. Bulk network rearrangement leads to gradual loss of connectivity in network. Network parameters: $L = 5 \mu m$, $l_c = 0.3 \mu m$, $\xi = 1 nN \cdot s/\mu m$, $v = 1 nN$. **b)** Simulation of an active network with fixed boundaries illustrating progressive buildup of internal stress through local filament rearrangement and deformation. Note the progressive buildup of compressive stress on individual filaments. Network parameters same as (a) except $v = 0.1 nN$. **c)** Plots of total network stress and the average extensional (blue) and compressive (red) stress on individual filaments for the simulation shown in (a). Rapid buildup of extensional stress allows the network transiently to exert force on its boundary, but this force subsides as network connectivity breaks down. **d)** Plots of total network stress and the average extensional (blue) and compressive (red) stress on individual filaments for the simulation shown in (b). Rapid buildup of extensional stress allows the network transiently to exert force on its boundary, but this force is dissipated at longer times as internal extensional and compressive stresses become balanced. Different time scales are shown on the x-axis to illustrate that the force buildup timescale is similar for each even though the force falloff is quite different.

peak in steady state stress occurs when $\tau_r \approx \tau_{max}$, where τ_{max} is the time at which the active stress peaks in the absence of turnover. Indeed, we observed a close correspondence between the steady state stress for a particular value of τ_r , and the stress observed at time $t = \tau_r$ during the buildup and dissipation of active stress in the

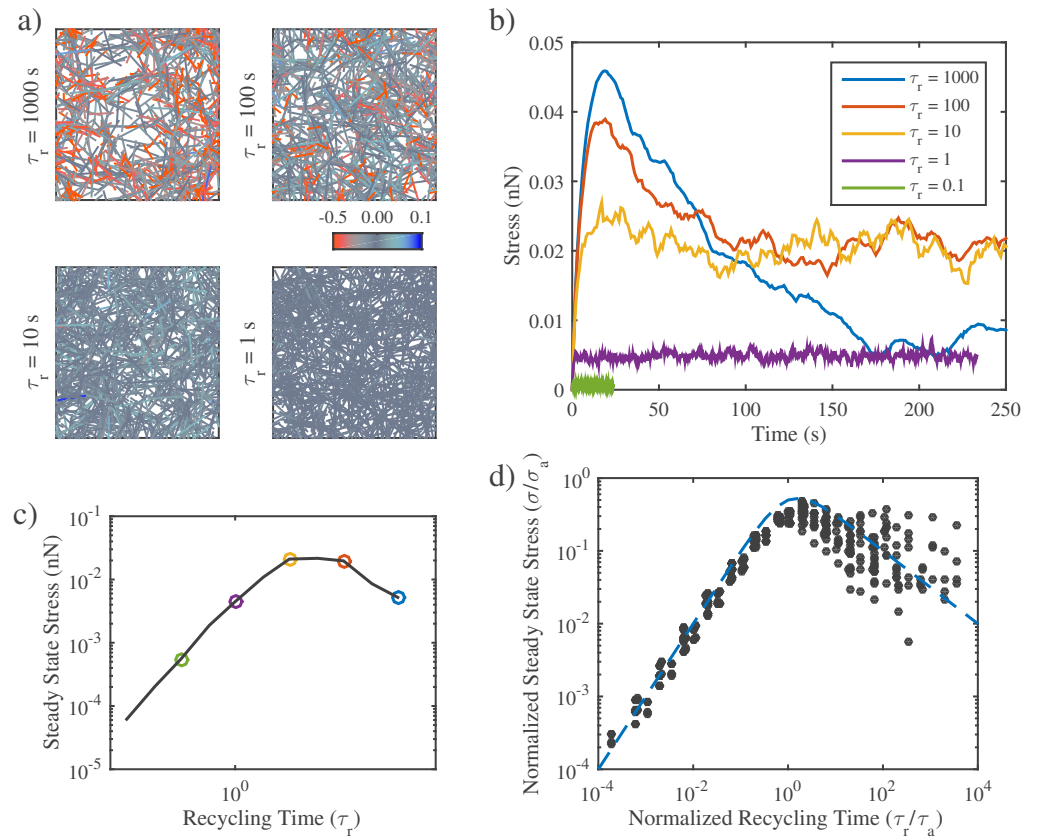


Figure 7. Filament recycling allows network to exert sustained stress on a fixed boundary. **a)** Snapshots from simulations of active networks with fixed boundaries for different timescales of filament recycling. Network parameters are the same as in Figure 6a. Note that significant remodeling occurs for longer recycling times. **b)** Plots of net stress exerted by the network on its boundaries for different recycling times; for long-lived filaments, stress is built rapidly, but then dissipates. Increasing filament turnover rates reduces stress dissipation by recycling compressed filaments; however, very short recycling times prevent any stress from being built up in the first place. **c)** Plotting the steady state stress derived from the long term stress values of the stress in panel b. **d)** Normalized steady state stress as a function of normalized recycling time. The steady state stress is set by the timescale at which the network strain is refreshed relative to the timescale at which the max stress is reached. The values have been normalized to the predicted peak stress, σ_{max} in the absence of recycling. Blue dashed line indicates the approximation given in equation 13 for $n = 1$.

absence of turnover. We observed a similar correspondence for the individual contributions of extensional and compressional stress.

We can understand the biphasic dependence of steady state stress on filament lifetime using the same reasoning applied to the case of passive flow: During steady state contraction, the average behavior of individual filaments is to build and dissipate active stress on approximately the same schedule as an entire network contracting from an initially unstressed state (Figure 7b). Therefore for $\tau_r < \tau_{max}$, increasing lifetime should increase the mean stress contributed by each filament. For $\tau_r > \tau_{max}$, further increases in lifetime should begin to reduce the mean stress contribution. Indeed, plotting normalized steady state stress (steady state stress/peak stress) vs normalized

recycling time (τ_c / τ_{max}) confirmed that this biphasic dependence of steady state stress on recycling times holds for a large range of sampled values of network parameters (Figure 7d). In particular, for $\tau_r < \tau_{max}$, the scaled data collapsed tightly onto a single curve representing a linear increase in steady state stress with increasing τ_r . For $\tau_r > \tau_{max}$, the scaling was less consistent, but the trend towards a monotonic decrease with increasing τ_r was clear.

As for the passive response (i.e. Equation 12), we can describe this biphasic dependence phenomenologically with an equation of the form:

$$\sigma_{ss} = \frac{\sigma_{peak}}{(\tau_r / \tau_{max})^n + \tau_{max} / \tau_r} \quad (13)$$

where the origins of the exponent n remain unclear.

Filament recycling tunes the balance between active stress buildup and viscous stress relaxation to generate flows

Thus far, we have considered independently how network remodeling controls the passive response to an external stress, or the steady state stress produced by active contraction against an external resistance. We now consider how these two forms of dependence will combine to shape steady state flow produced by spatial gradients of motor activity. To do so, we consider a simple scenario in which a network is pinned on either side and motor activity is continuously patterned such that the right half network has uniformly high levels of motor activity (controlled by v , with $\psi = 0.5$), while the left half network has none. Under these conditions, the right half network will contract continuously against a passive resistance from the left half network. Note that because of asymmetric filament compliance (EMM: is this sufficient argument, or do we need more?), the internal resistance of the right half network to active compression is small compared to the external resistance of the left half network. Thus the steady state flow will be described by:

$$\dot{\gamma} = \frac{\sigma_{ss}}{\eta_r} \quad (14)$$

where σ_{ss} is the active stress generated by the right half-network (less the internal resistance to filament compression), η_r is the effective viscosity of the left half network and strain rate $\dot{\gamma}$ is measured in the left half-network. Note that strain rate can be converted into a flow velocity v at the boundary between right and left halves through $v = \dot{\gamma} D x$. Therefore, we can understand the dependence of flow speed on filament turnover and other parameters via the approximate relationships summarized by equations 12 and 13 for η and σ_{ss} . As shown in Figure 8, there are two qualitatively distinct cases for the dependence of strain rate on τ_r , depending on the relative magnitudes of τ_{max} and τ_c . For both cases, we expect weak dependence of strain rate on τ_r for low τ_r (where both η and σ_{ss} show similar dependence on τ_r), and a sharp decrease in strain rate with increasing τ_r for very large τ_r , (where η is insensitive and σ_{ss} falls off sharply with τ_r). For $\tau_{max} < \tau_c$, we predict a peak strain rate at intermediate recycling times followed by a rapid falloff at lower recycling times, whereas for $\tau_{max} > \tau_c$, we expect a more rapid approach to maximum strain rate and a slower fall off at lower recycling times. For all parameter values sampled in this study (chosen to lie in a physiological range), the condition $\tau_c > \tau_{max}$ was satisfied.

To confirm this prediction, we simulated the simple scenario described above for a range of values of τ_r , with all other parameter values initially fixed. As expected, we observed a sharp dependence of steady flow on filament recycling rate (Figure 9b,c). For very long recycling times, ($\tau_r = 1000s$, dark blue line), there was a rapid initial deformation (contraction of the active domain and dilation of the passive domain),

followed by a slow approach to a steady state flow characterized by slow contraction of the right half-domain and a matching dilation of the left half-domain (see S5 Fig). However, with decreasing values of τ_r , steady state flow speeds increased steadily, before reaching an approximate plateau on which flow speeds varied by less than 15 % over more than two decades of variation in τ_r . (Figure 9c). Repeating these simulations for a wider range of parameter values and plotting normalized strain rate vs normalized τ_r (EMM: need to work through and describe the origins of this scaling) confirmed that the basic dependence predicted above holds more generally.

A final paragraph about scaling blah blah?

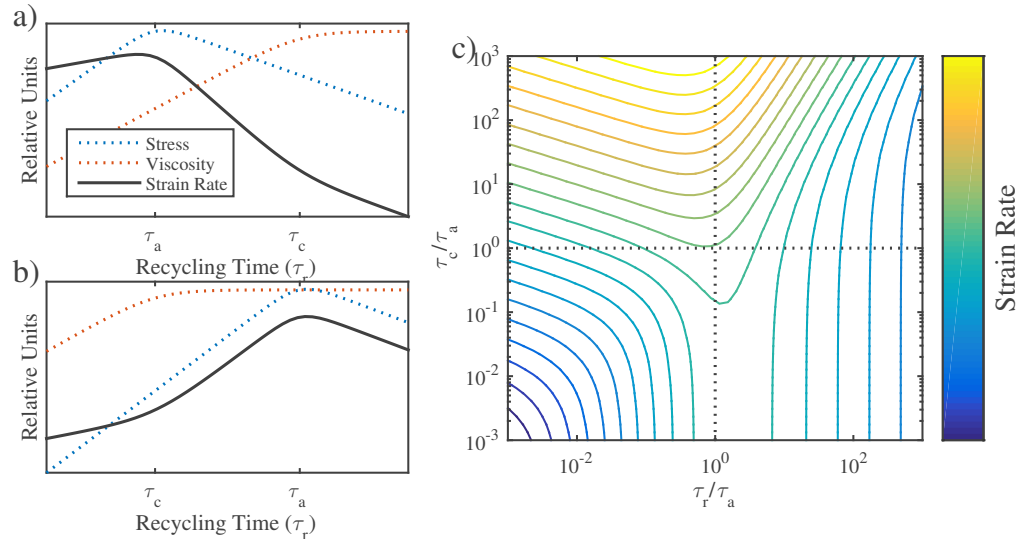


Figure 8. Filament recycling tunes the magnitudes of both effective viscosity and steady state stress. **a)** Dependence of steady state stress, effective viscosity, and resulting strain rate on recycling time τ_r under the condition $\tau_{max} < \tau_c$. **b)** Same as a) but for $\tau_c < \tau_{max}$. **c)** State space of flow rate dependence relative to the two relaxation timescales, τ_r and τ_c normalized by the stress buildup timescale, τ_{max} .

Conclusion

Our work aimed to create a simulation framework that would allow us to analyze the origins of macroscopic flow in terms of a handful of physiologically relevant microscopic parameters. Toward this aim we developed a minimalist model of a 2D filament network and analyzed the network's reaction to a variety of situations. We found mathematical relationships that determined both the passive effective viscosity and the active stress generation of networks with and without recycling. From these relationships we were able to make predictions about the rates of network flow in non-isotropic networks mimicking those found in polarized eukaryotic actomyosin cortices.

Importantly, our work brings a theoretical understanding to the importance of actomyosin turnover in producing and maintaining long-term large scale flows. We propose the concept of “filament recycling” to refer to the multitude of biochemical interactions which can give rise to the piece by piece architectural resetting of filament networks. We believe that our analysis of networks in the presence of this filament recycling will be useful in further developing the qualitative and quantitative understanding the deformation of these complex networks.

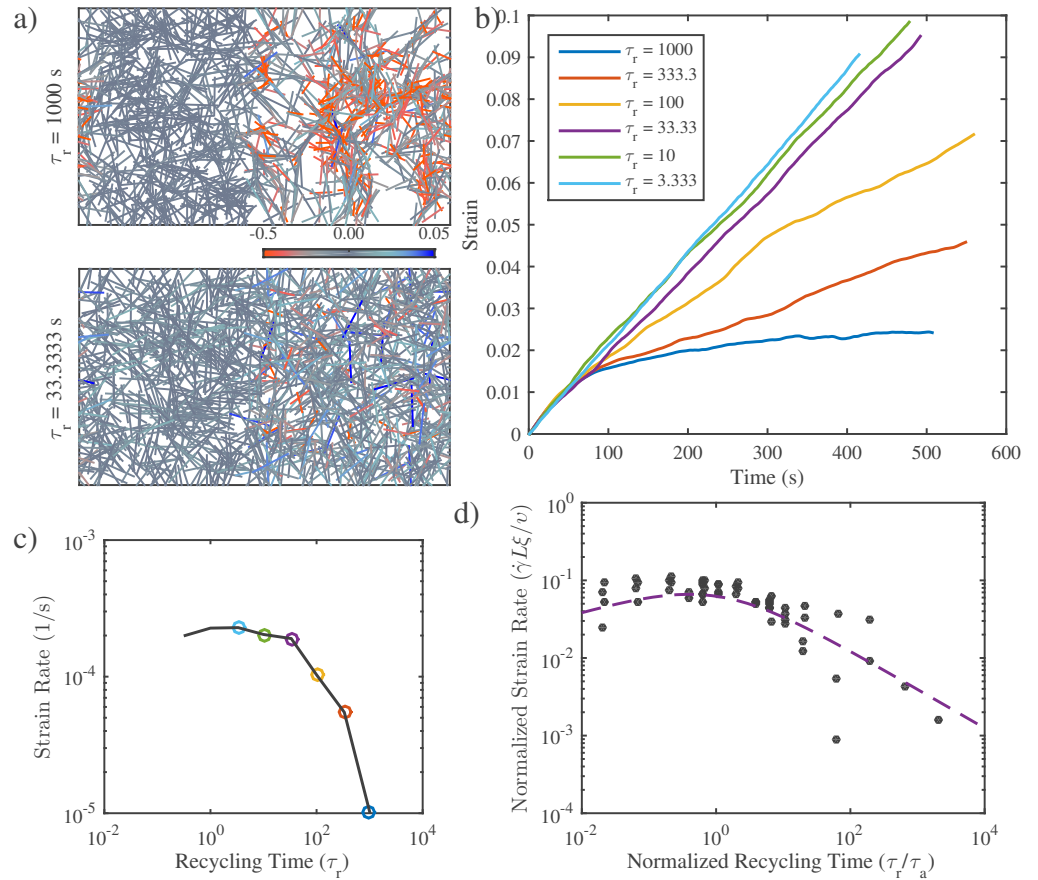


Figure 9. Filament recycling allows sustained flows in networks with non-isotropic activity. **a)** Example simulations of non-isotropic networks with long ($\tau_r = 1000$) and short ($\tau_r = 33$) recycling timescales. In these networks the left half of the network is passive while the right half is active. Network parameters are same as in Figures 6 and 7. Importantly, in all simulations $\tau_{max} < \tau_c$. **b)** Graph of strain for identical networks with varying recycling timescales. With long recycling times, the network stalls; reducing the recycling timescale allows the network to persist in its deformation. However, for the shortest recycling timescales, the steady state strain begins to slowly return to 0 net motion. Measurements are based on the passive side of the network. **c)** Steady state strain rates for the networks in (b). **d)** Graph of network's long-term strain rate as a function of recycling timescale. Dashed line is predicted form of dependence from theoretical argument in Figure 8.

Supporting Information

S1 Text. Supplementary Methods. Derivations of effective viscosity and critical recycling timescale.

S1 Table. Parameter values. List of parameter values used for each set of simulations.

S1 Fig. Filament recycling rescues strain thinning. **a)** Example networks with different levels of filament recycling. **b)** Strain curves for networks in (a). Note that the

networks with faster recycling have higher strain rates and that their strain rates appear more constant than the $\tau_r = \infty$ case. **c)** Graph of filament density vs strain for the networks in (a). Note that networks with recycling appear to reach steady state densities, while the network without recycling continues to thin until it tore at 80% strain.

S2 Fig. Mechanical properties of active networks **a)** Timescale of maximum strain in networks free to contract. This relationship was found phenomenologically. **b)** The network's ability to deform relies on the magnitude of asymmetric filament compliance. Total network strain also increases with the applied myosin force v . Note that the extent of contraction approaches an asymptotic limit as the stiffness asymmetry approaches a ratio of ~ 100 . **c)** Time at which the network reached its maximum stress. τ_a was found phenomenologically. **d)** Max stress of the network. Dependence was found phenomenologically.

S3 Fig. Tearing of active networks is prevented via recycling. **a)** An active network undergoing large scale deformations due to active filament rearrangements. **b)** The same network as in a) but with a shorter filament recycling time. **c)** Time trace of internal stresses for network in panel a. **d)** Time trace of internal stresses for network in panel b.

S4 Fig. Bimodal recycling dependence mirrors bimodal stress buildup. **a)** Bimodal buildup of stress in a network with long filament lifetime ($\tau_r = 1000s$). **b)** Steady state stress for networks with same parameters as in a) with varying recycling times.

S5 Fig. Stress and strain profiles of networks with contractile and passive domains. **a)** Blue line indicates strain velocity profile while orange represents net stress as measured in the main text. **b)** Same as panel a except for the condition where recycling time is 10 s. Note the increase in net stress and the corresponding increase in flow rate.

S1 Video. Extensional strain in passive networks. Movie of simulation setup shown in Figure 2. Colors are same as in figure.

S2 Video. Active networks contracting with free boundaries. Movie of simulation setup shown in Figure 5. Colors are same as in figure.

Acknowledgments

We would like to thank Shiladitya Banerjee and Patrick McCall for stimulating discussions.

References

Alvarado et al., 2013. Alvarado, J., Sheinman, M., Sharma, A., MacKintosh, F. C., and Koenderink, G. H. (2013). Molecular motors robustly drive active gels to a critically connected state. *Nat Phys*, 9(9):591–597.

-
- Banerjee et al., 2011. Banerjee, S., Marchetti, M. C., and Müller-Nedebock, K. (2011). Motor-driven dynamics of cytoskeletal filaments in motility assays. *Phys. Rev. E*, 84:011914.
- Bausch et al., 1998. Bausch, A. R., Ziemann, F., Boulbitch, A. A., Jacobson, K., and Sackmann, E. (1998). Local measurements of viscoelastic parameters of adherent cell surfaces by magnetic bead microrheometry. *Biophysical Journal*, 75(4):2038 – 2049.
- Bendix et al., 2008. Bendix, P. M., Koenderink, G. H., Cuvelier, D., Dogic, Z., Koeleman, B. N., Briehar, W. M., Field, C. M., Mahadevan, L., and Weitz, D. A. (2008). A quantitative analysis of contractility in active cytoskeletal protein networks. *Biophysical Journal*, 94(8):3126 – 3136.
- Benink et al., 2000. Benink, H. A., Mandato, C. A., and Bement, W. M. (2000). Analysis of cortical flow models in vivo. *Molecular Biology of the Cell*, 11(8):2553–2563.
- Bois et al., 2011. Bois, J. S., Jülicher, F., and Grill, S. W. (2011). Pattern formation in active fluids. *Phys. Rev. Lett.*, 106:028103.
- Bray and White, 1988. Bray, D. and White, J. (1988). Cortical flow in animal cells. *Science*, 239(4842):883–888.
- Broedersz et al., 2010. Broedersz, C. P., Depken, M., Yao, N. Y., Pollak, M. R., Weitz, D. A., and MacKintosh, F. C. (2010). Cross-link-governed dynamics of biopolymer networks. *Phys. Rev. Lett.*, 105:238101.
- Broedersz et al., 2009. Broedersz, C. P., Storm, C., and MacKintosh, F. C. (2009). Effective-medium approach for stiff polymer networks with flexible cross-links. *Phys. Rev. E*, 79:061914.
- Carlsson, 2010. Carlsson, A. E. (2010). Actin dynamics: From nanoscale to microscale. *Annual review of biophysics*, 39:91–110.
- Chandran and Mofrad, 2010. Chandran, P. L. and Mofrad, M. R. K. (2010). Averaged implicit hydrodynamic model of semiflexible filaments. *Phys. Rev. E*, 81:031920.
- Chugh et al., 2016. Chugh, P., Clark, A. G., Smith, M. B., Cassani, D. A. D., Charras, G., Salbreux, G., and Paluch, E. K. (2016). Nanoscale organization of the actomyosin cortex during the cell cycle. *Biophysical Journal*, 110(3):198a.
- De La Cruz, 2009. De La Cruz, E. M. (2009). How cofilin severs an actin filament. *Biophysical reviews*, 1(2):51–59.
- De La Cruz and Gardel, 2015. De La Cruz, E. M. and Gardel, M. L. (2015). Actin mechanics and fragmentation. *Journal of Biological Chemistry*, 290(28):17137–17144.
- Dierkes et al., 2014. Dierkes, K., Sumi, A., Solon, J., and Salbreux, G. (2014). Spontaneous oscillations of elastic contractile materials with turnover. *Phys. Rev. Lett.*, 113:148102.
- Ennomani et al., 2016. Ennomani, H., Letort, G., Guérin, C., Martiel, J.-L., Cao, W., Nédélec, F., Cruz, E. M. D. L., Théry, M., and Blanchoin, L. (2016). Architecture and connectivity govern actin network contractility. *Current Biology*, 26(5):616 – 626.

-
- Evans and Yeung, 1989. Evans, E. and Yeung, A. (1989). Apparent viscosity and cortical tension of blood granulocytes determined by micropipet aspiration. *Biophysical Journal*, 56(1):151–160.
- Filippov et al., 2004. Filippov, A. E., Klafter, J., and Urbakh, M. (2004). Friction through dynamical formation and rupture of molecular bonds. *Phys. Rev. Lett.*, 92:135503.
- Fritzsche et al., 2016. Fritzsche, M., Erlenkämper, C., Moeendarbary, E., Charras, G., and Kruse, K. (2016). Actin kinetics shapes cortical network structure and mechanics. *Science Advances*, 2(4).
- Fritzsche et al., 2013. Fritzsche, M., Lewalle, A., Duke, T., Kruse, K., and Charras, G. (2013). Analysis of turnover dynamics of the submembranous actin cortex. *Molecular Biology of the Cell*, 24(6):757–767.
- Head et al., 2003. Head, D. A., Levine, A. J., and MacKintosh, F. C. (2003). Deformation of cross-linked semiflexible polymer networks. *Phys. Rev. Lett.*, 91:108102.
- Heisenberg and Bellaïche, 2013. Heisenberg, C.-P. and Bellaïche, Y. (2013). Forces in tissue morphogenesis and patterning. *Cell*, 153(5):948 – 962.
- Hiraiwa and Salbreux, 2015. Hiraiwa, T. and Salbreux, G. (2015). Role of turn-over in active stress generation in a filament network. *ArXiv e-prints*.
- Hird and White, 1993. Hird, S. N. and White, J. G. (1993). Cortical and cytoplasmic flow polarity in early embryonic cells of *Caenorhabditis elegans*. *The Journal of Cell Biology*, 121(6):1343–1355.
- Hochmuth, 2000. Hochmuth, R. M. (2000). Micropipette aspiration of living cells. *Journal of Biomechanics*, 33(1):15 – 22.
- Janson et al., 1991. Janson, L. W., Kolega, J., and Taylor, D. L. (1991). Modulation of contraction by gelation/solution in a reconstituted motile model. *The Journal of Cell Biology*, 114(5):1005–1015.
- Keren et al., 2009. Keren, K., Yam, P. T., Kinkhabwala, A., Mogilner, A., and Theriot, J. A. (2009). Intracellular fluid flow in rapidly moving cells. *Nat Cell Biol*, 11(10):1219–1224.
- Kim et al., 2014. Kim, T., Gardel, M. L., and Munro, E. (2014). Determinants of fluidlike behavior and effective viscosity in cross-linked actin networks. *Biophysical Journal*, 106(3):526 – 534.
- Kim et al., 2011. Kim, T., Hwang, W., and Kamm, R. D. (2011). Dynamic role of cross-linking proteins in actin rheology. *Biophysical Journal*, 101(7):1597–1603.
- Koenderink et al., 2009. Koenderink, G. H., Dogic, Z., Nakamura, F., Bendix, P. M., MacKintosh, F. C., Hartwig, J. H., Stossel, T. P., and Weitz, D. A. (2009). An active biopolymer network controlled by molecular motors. *Proceedings of the National Academy of Sciences of the United States of America*, 106(36):15192–15197.
- Lai et al., 2008. Lai, F. P., Szczodrak, M., Block, J., Faix, J., Breitsprecher, D., Mannherz, H. G., Stradal, T. E., Dunn, G. A., Small, J. V., and Rottner, K. (2008). Arp2/3 complex interactions and actin network turnover in lamellipodia. *The EMBO Journal*, 27(7):982–992.

-
- Lenz, 2014. Lenz, M. (2014). Geometrical origins of contractility in disordered actomyosin networks. *Phys. Rev. X*, 4:041002.
- Lenz et al., 2012. Lenz, M., Gardel, M. L., and Dinner, A. R. (2012). Requirements for contractility in disordered cytoskeletal bundles. *New Journal of Physics*, 14(3):033037.
- Lieleg and Bausch, 2007. Lieleg, O. and Bausch, A. R. (2007). Cross-linker unbinding and self-similarity in bundled cytoskeletal networks. *Phys. Rev. Lett.*, 99:158105.
- Lieleg et al., 2008. Lieleg, O., Claessens, M. M. A. E., Luan, Y., and Bausch, A. R. (2008). Transient binding and dissipation in cross-linked actin networks. *Phys. Rev. Lett.*, 101:108101.
- Lieleg et al., 2009. Lieleg, O., Schmoller, K. M., Claessens, M. M. A. E., and Bausch, A. R. (2009). Cytoskeletal polymer networks: Viscoelastic properties are determined by the microscopic interaction potential of cross-links. *Biophysical Journal*, 96(11):4725–4732.
- Liu et al., 2007. Liu, J., Koenderink, G. H., Kasza, K. E., MacKintosh, F. C., and Weitz, D. A. (2007). Visualizing the strain field in semiflexible polymer networks: Strain fluctuations and nonlinear rheology of *f*-actin gels. *Phys. Rev. Lett.*, 98:198304.
- Mak et al., 2016. Mak, M., Zaman, M. H., Kamm, R. D., and Kim, T. (2016). Interplay of active processes modulates tension and drives phase transition in self-renewing, motor-driven cytoskeletal networks. *Nat Commun*, 7.
- Marchetti et al., 2013. Marchetti, M. C., Joanny, J. F., Ramaswamy, S., Liverpool, T. B., Prost, J., Rao, M., and Simha, R. A. (2013). Hydrodynamics of soft active matter. *Rev. Mod. Phys.*, 85:1143–1189.
- Mayer et al., 2010. Mayer, M., Depken, M., Bois, J. S., Julicher, F., and Grill, S. W. (2010). Anisotropies in cortical tension reveal the physical basis of polarizing cortical flows. *Nature*, 467(7315):617–621.
- McCrum et al., 1997. McCrum, N., Buckley, C., and Bucknall, C. (1997). *Principles of Polymer Engineering*. Oxford science publications. Oxford University Press.
- Müller et al., 2014. Müller, K. W., Bruinsma, R. F., Lieleg, O., Bausch, A. R., Wall, W. A., and Levine, A. J. (2014). Rheology of semiflexible bundle networks with transient linkers. *Phys. Rev. Lett.*, 112:238102.
- Munjal et al., 2015. Munjal, A., Philippe, J.-M., Munro, E., and Lecuit, T. (2015). A self-organized biomechanical network drives shape changes during tissue morphogenesis. *Nature*, 524(7565):351–355.
- Murrell and Gardel, 2014. Murrell, M. and Gardel, M. L. (2014). Actomyosin sliding is attenuated in contractile biomimetic cortices. *Molecular Biology of the Cell*, 25(12):1845–1853.
- Murrell et al., 2015. Murrell, M., Oakes, P. W., Lenz, M., and Gardel, M. L. (2015). Forcing cells into shape: the mechanics of actomyosin contractility. *Nat Rev Mol Cell Biol*, 16(8):486–498.
- Murrell and Gardel, 2012. Murrell, M. P. and Gardel, M. L. (2012). F-actin buckling coordinates contractility and severing in a biomimetic actomyosin cortex. *Proceedings of the National Academy of Sciences*, 109(51):20820–20825.

-
- Nedelec et al., 1997. Nedelec, F. J., Surrey, T., Maggs, A. C., and Leibler, S. (1997). Self-organization of microtubules and motors. *Nature*, 389(6648):305–308.
- Reymann et al., 2012. Reymann, A.-C., Boujemaa-Paterski, R., Martiel, J.-L., Guérin, C., Cao, W., Chin, H. F., De La Cruz, E. M., Théry, M., and Blanchoin, L. (2012). Actin network architecture can determine myosin motor activity. *Science*, 336(6086):1310–1314.
- Salbreux et al., 2012. Salbreux, G., Charras, G., and Paluch, E. (2012). Actin cortex mechanics and cellular morphogenesis. *Trends in Cell Biology*, 22(10):536 – 545.
- Salbreux et al., 2009. Salbreux, G., Prost, J., and Joanny, J. F. (2009). Hydrodynamics of cellular cortical flows and the formation of contractile rings. *Phys. Rev. Lett.*, 103:058102.
- Sanchez et al., 2012. Sanchez, T., Chen, D. T. N., DeCamp, S. J., Heymann, M., and Dogic, Z. (2012). Spontaneous motion in hierarchically assembled active matter. *Nature*, 491(7424):431–434.
- Spruijt et al., 2010. Spruijt, E., Sprakel, J., Lemmers, M., Stuart, M. A. C., and van der Gucht, J. (2010). Relaxation dynamics at different time scales in electrostatic complexes: Time-salt superposition. *Phys. Rev. Lett.*, 105:208301.
- Surrey et al., 2001. Surrey, T., Nédélec, F., Leibler, S., and Karsenti, E. (2001). Physical properties determining self-organization of motors and microtubules. *Science*, 292(5519):1167–1171.
- Turlier et al., 2014. Turlier, H., Audoly, B., Prost, J., and Joanny, J.-F. (2014). Furrow constriction in animal cell cytokinesis. *Biophysical Journal*, 106(1):114 – 123.
- Unterberger and Holzapfel, 2014. Unterberger, M. J. and Holzapfel, G. A. (2014). Advances in the mechanical modeling of filamentous actin and its cross-linked networks on multiple scales. *Biomechanics and Modeling in Mechanobiology*, 13(6):1155–1174.
- Van Goor et al., 2012. Van Goor, D., Hyland, C., Schaefer, A. W., and Forscher, P. (2012). The role of actin turnover in retrograde actin network flow in neuronal growth cones. *PLoS ONE*, 7(2):e30959.
- Vanossi et al., 2013. Vanossi, A., Manini, N., Urbakh, M., Zapperi, S., and Tosatti, E. (2013). *Colloquium* : Modeling friction: From nanoscale to mesoscale. *Rev. Mod. Phys.*, 85:529–552.
- Wachsstock et al., 1994. Wachsstock, D., Schwarz, W., and Pollard, T. (1994). Cross-linker dynamics determine the mechanical properties of actin gels. *Biophysical Journal*, 66(3, Part 1):801 – 809.
- Ward et al., 2015. Ward, A., Hilitski, F., Schwenger, W., Welch, D., Lau, A. W. C., Vitelli, V., Mahadevan, L., and Dogic, Z. (2015). Solid friction between soft filaments. *Nat Mater*, advance online publication:–.
- Wilhelm and Frey, 2003. Wilhelm, J. and Frey, E. (2003). Elasticity of stiff polymer networks. *Phys. Rev. Lett.*, 91:108103.
- Wilson et al., 2010. Wilson, C. A., Tsuchida, M. A., Allen, G. M., Barnhart, E. L., Applegate, K. T., Yam, P. T., Ji, L., Keren, K., Danuser, G., and Theriot, J. A. (2010). Myosin ii contributes to cell-scale actin network treadmilling through network disassembly. *Nature*, 465(7296):373–377.

-
- Yao et al., 2011. Yao, N. Y., Becker, D. J., Broedersz, C. P., Depken, M., MacKintosh, F. C., Pollak, M. R., and Weitz, D. A. (2011). Nonlinear viscoelasticity of actin transiently cross-linked with mutant alpha-actinin-4. *Journal of Molecular Biology*, 411(5):1062 – 1071.
- Zumdieck et al., 2007. Zumdieck, A., Kruse, K., Bringmann, H., Hyman, A. A., and Jülicher, F. (2007). Stress generation and filament turnover during actin ring constriction. *PLoS ONE*, 2(8):e696.